PAPER

Magnetically recoverable ZrO$_2$/Fe$_3$O$_4$/chitosan nanomaterials for enhanced sunlight driven photoreduction of carcinogenic Cr(VI) and dechlorination & mineralization of 4-chlorophenol from simulated waste water†

Amit Kumar,*[a] Changsheng Guo,[d] Gaurav Sharma,[a] Deepak Pathania,[a] Mu Naushad,[c] Susheel Kalia[b] and Pooja Dhiman[e]

In this laboratory-scale experiment we report the treatment of carcinogenic Cr(VI) and 4-chlorophenol by ferromagnetic ZrO$_2$/Fe$_3$O$_4$ nano-heterojunctions supported on chitosan. A combination of different semiconductors with different photo-activities has proven to be a tested and effective technique for harnessing solar light in waste water treatment. The prepared heterojunction and its composite with chitosan has been characterized by X-Ray Diffraction (XRD), Fourier Transform Infra Red spectroscopy (FTIR), High Resolution Transmission Electron Microscopy (HRTEM), Small Area Electron Diffraction (SAED), Vibrating Sample Magnetometry (VSM), Energy Dispersive X-ray analysis (EDX), UV-visible spectrophotometry and Brunauer–Emmet–Teller surface area analysis (BET). Treatment of chlorophenols is challenging because of their hydrophobicity and stability. In our study we have reported excellent results for the dechlorination of 4-chlorophenol and the results were analyzed in terms of Liquid Chromatography-Mass Spectrometry (LC-MS), Chemical Oxygen Demand analysis (COD) and emission. 88.6% of 4-CP degradation was achieved in the presence of ZrO$_2$/Fe$_3$O$_4$/chitosan in 3 h under sunlight and a reduction of 90.2% for Cr(VI) was obtained. The heterojunction formation leads to charge separation and decreased recombination of charge carriers. The synergistic effects of charge separation in the heterojunction, alcohols, peroxide, magnetism and adsorption with essential explanation of mechanisms make this study important and promising.

1. Introduction

Harnessing of solar energy for the removal of persistent pollutants from water systems with an economically viable method has remained a major challenge. The deterioration of the environment and growing demand for fresh and clean water

[a]*School of Chemistry, Shoolini University, Solan, Himachal Pradesh, 173212, India. E-mail: mittuchem83@gmail.com; Tel: +91 9625310313*

[b]*Department of Chemistry, Army Cadet College Wing, Indian Military Academy, Dehradun – 248007, UK, India*

[c]*Department of Chemistry, College of Science, King Saud University, Building#5, Riyadh, Saudi Arabia*

[d]*State Key Laboratory of Environmental Criteria and Risk Assessment, Chinese Research Academy of Environmental Sciences, Beijing, China, 100012*

[e]*Department of Physics, IEC University, Solan, Himachal Pradesh, India*

† Electronic supplementary information (ESI) available: Digital photographs of magnetic separation and decolorisation of DPC-Cr(VI) (Fig. S1), absorption spectrum of 4-CP with time in the presence of ZFC under solar light (Fig. S2), adsorption of 4-CP onto ZF and ZFC in the dark experiment (Fig. S3a), influence of initial pH on the degradation of 4-CP in the presence of ZFC under solar light (Fig. S4). See DOI: 10.1039/c5ra23372k

has given rise to the search for new hybrid nanomaterials. Among various applications of semiconductor nanoparticles, photocatalysis has been most exploited[1–4] due to its efficiency, potential and cost-effectiveness. The photocatalytic efficiency can be enhanced by optimizing the lifetime of charge carriers or by minimizing the electron–hole combinations. One such strategy is the formation of mixed or coupled semiconductors or the formation of heterojunctions. Coupled semiconductors or nano-heterostructures have been found to be highly beneficial in the removal of various organic and inorganic pollutants using advanced oxidation processes.[5–9] Magnetic nanoparticles consisting of semiconductors, especially iron oxides, have been widely used in low cost adsorption, photocatalysis, and drug delivery *etc.*[10] The current need is to remove the resistant contaminants with novel materials through adsorption, advance oxidation processes (AOPs), magnetic recovery and sensitization. Conversion of harmful organic and inorganic wastes into ones with low toxicity in aqueous solutions under mild conditions is one of the most promising techniques. Among various notorious pollutants hexavalent chromium (Cr(VI)) is the one which is released frequently into waste water

by tanning and painting industries.[11,12] Its removal from waste water is of crucial importance because it is carcinogenic and can easily get into the food chain.[13–15] One of the most preferred methods to treat Cr(VI) in waste water is the transformation of Cr(VI) to Cr(III).

This is an essential characteristic of photocatalytic technology for water treatment because the toxicity of inorganic substances depends on their oxidation state. For example, photocatalysis can reduce Cr(VI)[16,17] to Cr(III) which is significantly less toxic and can be easily precipitated during a reaction as $Cr(OH)_3$ as a solid waste.[18]

Among other pollutants, chlorophenols represent an important class of intensively researched pollutants.[19–22] Chlorophenols are one of the priority pollutants as per the U.S. EPA.[23] 4-Chlorophenol (4-CP) is used in pharmaceuticals, dyes, explosives, disinfectants and antiseptics. It is a highly toxic pollutant[24,25] which is carcinogenic and mutagenic too. The disposal of chlorophenols, bromophenols, and nitrophenols *etc.* has been a matter of serious concern according to environmental standards. Various methods have been employed for its remediation *viz.* adsorption, microbial degradation, chemical oxidation and photocatalytic removal. Removal of phenols by environmental friendly and cost effective photo-oxidation and dechlorination has remained most promising and convincing.

Various coupled metal oxides and heterojunctions such as $ZnO–TiO_2$,[26] $TiO_2–Fe_3O_4$,[27] $Fe_3O_4–Cr_2O_3$,[28] $TiO_2–Cu_2S$[29] and $ZnO–ZnSe$[30] have been used by researchers worldwide for photocatalytic removal of various pollutants. Due to its lower band gap of 2.2 eV and magnetism, Fe_3O_4 makes an interesting candidate for heterojunction formation. Fe_3O_4-based nanomaterials have been successfully used in waste water treatment as they are cost effective and possess adsorption capacity, biocompatibility, visible region absorption and stability.[31–34] In addition, in combination with H_2O_2, it forms a Fenton system which is highly efficient in the production of reactive oxygen species.

Nano ZrO_2 finds roles in various applications of nanomaterials[35–37] due to its crystallinity, semiconductor behavior, tunable structural and morphological properties and long life span. ZrO_2 exists in polymorphs as monoclinic, tetragonal, and cubic phases. A lot of work has been reported for the degradation of phenols and Cr(VI) photoreduction using various nanomaterials. The special interest in this laboratory-level experiment is the synthesis of magnetic ZrO_2/Fe_3O_4 heterostructures supported on chitosan and used for Cr(VI) photoreduction and 4-chlorophenol degradation. The synergism between adsorption, photocatalysis, pH, the presence of alcohol, scavenger and magnetic properties brings out a promising magnetically recoverable nanomaterial with high recycling efficiency.

2. Materials and methods

2.1 Materials

Analytical grade zirconium oxychloride, ferrous chloride, ferric chloride, ammonium hydroxide, chitosan, 4-chlorophenol (4-CP), potassium dichromate, hydrogen peroxide, isopropanol, and ethanol were acquired from Sigma Aldrich and used without any further purification.

2.2 Synthesis of photocatalysts ZrO_2/Fe_3O_4 (ZF)

Fe_3O_4 nanoparticles were synthesized by co-precipitation of Fe^{2+} and Fe^{3+} with NH_4OH by the usual reported method.[38] 0.1 g of synthesized Fe_3O_4 nanoparticles was dispersed in a solution containing 20% ethanol and 80% distilled water. 1 mL of NH_3 solution was added and stirred for 1 h. To this solution, an aqueous solution of $ZrOCl_2$ and 30% NH_3 was added. After 3 h of stirring the solution was refluxed. The obtained nanoparticles were filtered and sintered at 200 °C for 2 h.

2.3 Synthesis of $ZrO_2/Fe_3O_4/chitosan$ (ZFC)

0.5 g of chitosan was dissolved in a solution containing 20 mL ethanol and 80 mL distilled water. To this solution 0.1 g of the synthesized Fe_3O_4 nanoparticles was added and stirred for 2 h. To this solution an aqueous solution of $ZrOCl_2$ and NH_4OH solution was added and stirred for 3 h at room temperature. The filtered particles were washed with distilled water. The nanomaterials were vacuum dried at 80 °C.

2.4 Characterization

The crystal structure, phase purity and grain size of ZF and ZFC were obtained using an XPERTpro X-ray diffractometer. Scherrer's formula was employed to determine the crystallite size and Bragg's law was used for the *d*-spacing and lattice parameters. The FTIR spectra of the nanoparticles were recorded with the KBr pellet method using a Nicolet 5700 FTIR spectrometer. The SEM micrographs were taken with a LEO 435 VP instrument. A FEI Tecnai F20 transmission electron microscope was used for the high resolution transmission electron microscopy (HRTEM) images and for small area electron diffraction (SAED). Elemental analysis was done by an energy dispersive X-ray (EDX) spectroscopy instrument equipped with SEM. The ultraviolet-visible spectra (UV-vis) were recorded using a Systronics 2202 double beam spectrophotometer. Magnetic studies were carried out using a vibrating sample magnetometer (Microsense EV7, USA) up to a field of 10 000 Oe.

2.5 Optical/band gap studies

For computation of the optical band gap and band structure, a suspension of 5 mg of Fe_3O_4, ZrO_2, ZF and ZFC in ethanol was prepared. After ultrasonication of 1 h the UV-visible spectrum was obtained. The direct band gaps were then calculated using the Tauc relation.

2.6 BET studies

The Brunauer–Emmett–Teller (BET) surface areas of ZF and ZFC were determined using a NOVA 2200e Quantachrome set up over a relative pressure range of 0.05–0.90 using nitrogen as a purge gas.

2.7 Photoreduction of Cr(VI) under solar light

The photocatalytic activity of ZF and ZFC was tested using a carcinogenic Cr(VI) compound as the target pollutant in aqueous solution. All the experiments were performed under solar light. In a typical procedure 50 mg of the sample was added to 100 mL of $K_2Cr_2O_7$ solution (70 mg L^{-1}). The pH of the solution was maintained at 2. The solution was then kept in the dark to establish an adsorption–desorption equilibrium. Then the reaction system was exposed to direct sunlight (intensity 30 $\times 10^3 \pm 100$ lx). The Cr(VI) reduction was then evaluated spectrophotometrically (at $\lambda = 540$ nm) using the standard diphenylcarbazide (DPC) method.[39] The effect of pH, hydrogen peroxide and ethanol was also studied. The temperature of the system was maintained at 30 ± 0.5 °C in a double walled pyrex glass vessel containing the slurry and was surrounded by a thermostatic water circulation arrangement.

2.8 Photodegradation of 4-chlorophenol under solar illumination

The photocatalytic activity of the ZF and ZFC nanomaterials was tested against 4-chlorophenol as a target pollutant under natural sunlight. Prior to solar illumination, the photocatalyst (0.01 g) was added to 100 mL aqueous solution of 4-CP (20 mg L^{-1}) and kept in the dark with stirring to establish an adsorption–desorption equilibrium. The solution was placed in sunlight in a double walled cylinder with water circulation to keep the temperature constant. After fixed intervals of time an aliquot of solution was taken and the absorbance was recorded at 280 nm. The degradation results were also analyzed in terms of the decrease in chemical oxygen demand determined by the closed reflux method using potassium dichromate as the oxidant under acidic conditions. The unreacted oxidant was determined by titrating with ferrous ammonium sulphate using ferroin indicator.[40] After 1 h of degradation LC-MS was carried out. The liquid chromatography-mass spectrometry was carried out using QTOF LC-MS MS LC-MS, Waters, USA. The gradient HPLC separation was coupled with electrospray ionization (ESI)-mass spectrometry. The solvent used as the mobile phase was acetonitrile : water (1 : 1). The evolution of CO_2 was tested by a saturated $BaCl_2$ test.

2.9 Materials reuse

To study the reusability and effectiveness of ZF and ZFC for further use, the photocatalytic experiments for the photoreduction of Cr(VI) and degradation of 4-CP were performed for 6 continuous cycles. The experiments were of 2 h duration for Cr(VI) and 3 h for 4-CP.

3. Results and discussion

3.1 Characterization

3.1.1 FTIR analysis. Fig. 1a shows the FTIR spectrum of the ZrO_2/Fe_3O_4 nanoparticles (ZF). The peak at 470 cm^{-1},[41] 575 cm^{-1},[42] and 3410 cm^{-1} corresponds to the Zr–O, Fe–O and O–H stretching frequencies respectively. In the FTIR spectrum of ZrO_2/Fe_3O_4/chitosan (ZFC) the peaks for Zr–O and Fe–O are shifted to lower wavenumbers of 465 and 569 cm^{-1}. This may be due to bonding with the chitosan matrix. The peaks at 1114 cm^{-1}, 1589 cm^{-1}, and 3390 cm^{-1} are assigned to the C–O stretching, C=O stretching and O–H stretching vibrations for the chitosan moiety. This confirms the successful formation of ZF and ZFC.

3.1.2 XRD analysis. The XRD pattern of ZFC is given in Fig. 2. The peaks at $2\theta = 31.7°$, $35.18°$, $50.5°$ and $60.4°$ reveal the diffraction planes of (111), (200), (220) and (311) (marked in black) respectively which confirms the cubic form of ZrO_2 as per JCPDS file no. 27-0997.[43] Some additional peaks are also observed which are due to the simultaneous presence of monoclinic forms of ZrO_2. The peaks at 30.7°, 35.5°, 43.9°, 54.1°, and 63° correspond to the (220), (311), (400), (422) and (440) diffraction planes of the spinel cubic structure of Fe_3O_4 in good agreement with JCPDS file no. 65-3107.[44]

There may be some missing peaks both for ZrO_2 and Fe_3O_4 because of the presence of the chitosan matrix. In addition peaks below 30° represent diffraction due to chitosan chains.[45] The average crystallite size calculated for the ZFC nanoparticles is 27.3 nm using Bragg's diffraction law. The d-spacings for planes (220), (311), (400), (422), and (440) for Fe_3O_4 are 2.93, 2.63, 2.09, 1.79, and 1.48 Å, respectively. Similarly the d-spacings for the (111), (200), (220) and (311) planes for c-ZrO_2 are 2.81, 2.56, 1.82, and 1.51 Å respectively.

3.1.3 SEM/EDX analysis. The SEM images of ZF are represented in Fig. 3a and b at a lower and higher magnification. We see the uniform and spherical particle formation with porosity. In the SEM image of ZFC (Fig. 3c) the chitosan matrix with a rough surface is visible with metal oxide nanoparticles spread over it. The composite shows a higher hierarchy as compared to ZF. The EDX pattern of ZFC (Fig. 4a) shows the presence of Fe, Zr, O, C and N elements which confirms the formation of the ZFC nanocomposite.

3.1.4 Magnetic properties. The M–H curves for ZF and ZFC as obtained from the VSM studies are given in Fig. 4b and c respectively. The magnetization hysteresis loop of the ZF nanoparticles shows that the material exhibits a typical ferromagnetic behavior. The saturation magnetization (M_s) and the coercivity (H_c) are about 65 emu g^{-1}. It can also be inferred that the coercivity is also very low which shows that the material slightly lies in the superparamagnetic phase. The high H_c and M_s of the ZF nanocrystals can be attributed to the magnetic anisotropy of Fe_3O_4 which is easily separated from aqueous medium as represented in the inset of Fig. 4b. A similar behavior is shown by ZFC which exhibits a lower saturation magnetization of 42 emu g^{-1} which is lower than that of ZF but is actually quite high. The higher magnetization assures the faster and easy recovery of the materials.

3.1.5 Optical studies. The Tauc plots (Fig. 5a) as derived from the UV-visible spectra of Fe_3O_4, ZrO_2 and ZrO_2/Fe_3O_4 were obtained and the Tauc plots were plotted using the empirical relation:[46]

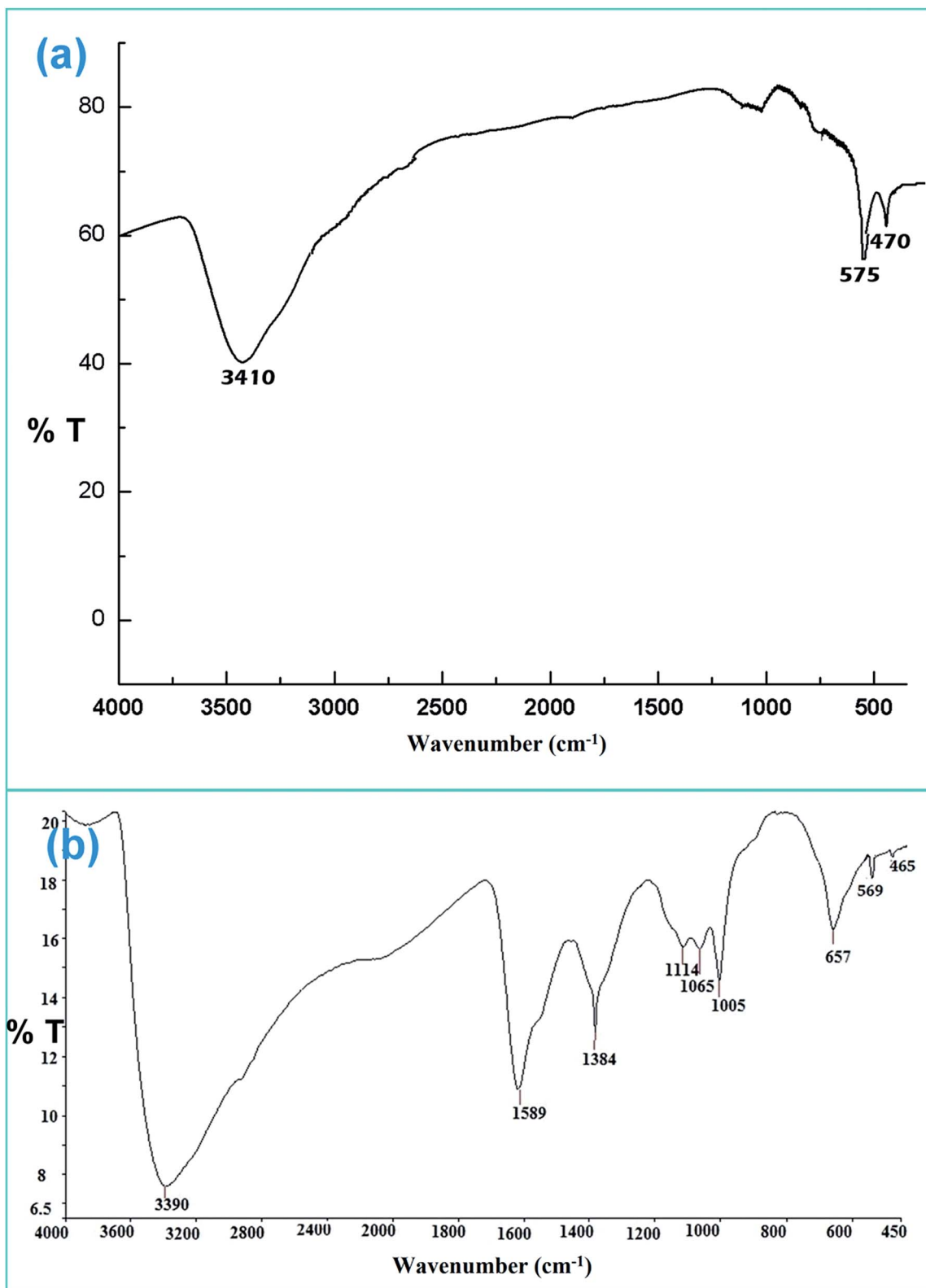$$\alpha h\nu = B(h\nu - E_g)^n \tag{1}$$

Fig. 1   FTIR spectrum of (a) ZF and (b) ZFC.

where α = absorption coefficient = $2.303A/l$, E_g = optical band gap, B = band tailing parameter, $h\nu$ = photon energy, and $n = 1/2$ for direct band gap semiconductors. The optical band gaps for ZrO_2, Fe_3O_4 and ZF are 3.01 eV, 2.22 eV and 2.52 eV respectively. The band gap of the heterostructure lies between that of Fe_3O_4 and ZrO_2.
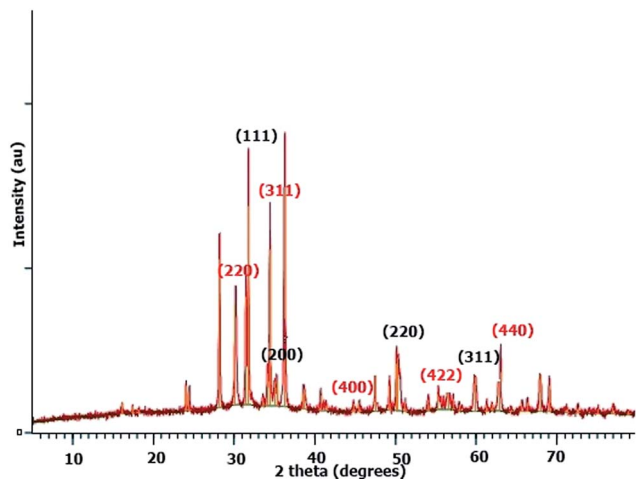
Fig. 2 XRD pattern of ZFC.

The energy bands of ZrO_2, Fe_3O_4 and ZFC were calculated using the following relation:[47]

$$E_{VB} = X - E^e + 0.5E_g \quad (2)$$

$$E_{CB} = E_{VB} - E_g \quad (3)$$

where E_{VB} and E_{CB} are the band edge potentials of the valence band and conduction band respectively, E^e is the energy of the electrons on the hydrogen scale (∼4.5 eV), X is the geometric mean of the absolute electronegativity of the constituent atoms on the Pearson scale (PAE), and E_g is the band gap of the semiconductor in electron volts. The band gaps and band edges as calculated are listed in Table 1.

Various experiments report that due to the formation of such a heterostructure there is a migration of charge carriers which eventually leads to a charge separation. Also the position of the band edges also leads to attraction of charge carriers which leads to accumulation of charges near the edges leading to charge separation. In all the above work it has been proven that semiconductor coupling leads to increased transport, charge separation and decreased recombination rate. The holes accumulate on to the VB of ZrO_2 because of a less positive band edge and similarly electrons accumulate near the CB of Fe_3O_4 because of the positive band edge (negative for ZrO_2). This eventually leads to decreased recombination and charge separation.

3.1.6 BET studies. The N_2 adsorption isotherms for ZF and ZFC are given in Fig. 5b and c respectively. The BET surface areas for ZF and ZFC are 92 and 211 m^2 g^{-1}, respectively. Thus the chitosan matrix helps to increase the surface area, provides stability and prevents the particle agglomeration.

3.1.7 TEM analysis. Transmission electron microscopy of different resolutions was applied to characterize the size and morphology of the ZF and ZFC nanomaterials. Fig. 6a represents the TEM images of the ZF nanoparticles. Well-shaped cubic and spherical particles were observed. The SAED pattern (Fig. 6a inset) shows that the ZF heterostructures are highly crystalline. The average particles size is 16–21 nm which is in agreement with the XRD data. The HRTEM image of ZF (Fig. 6b)
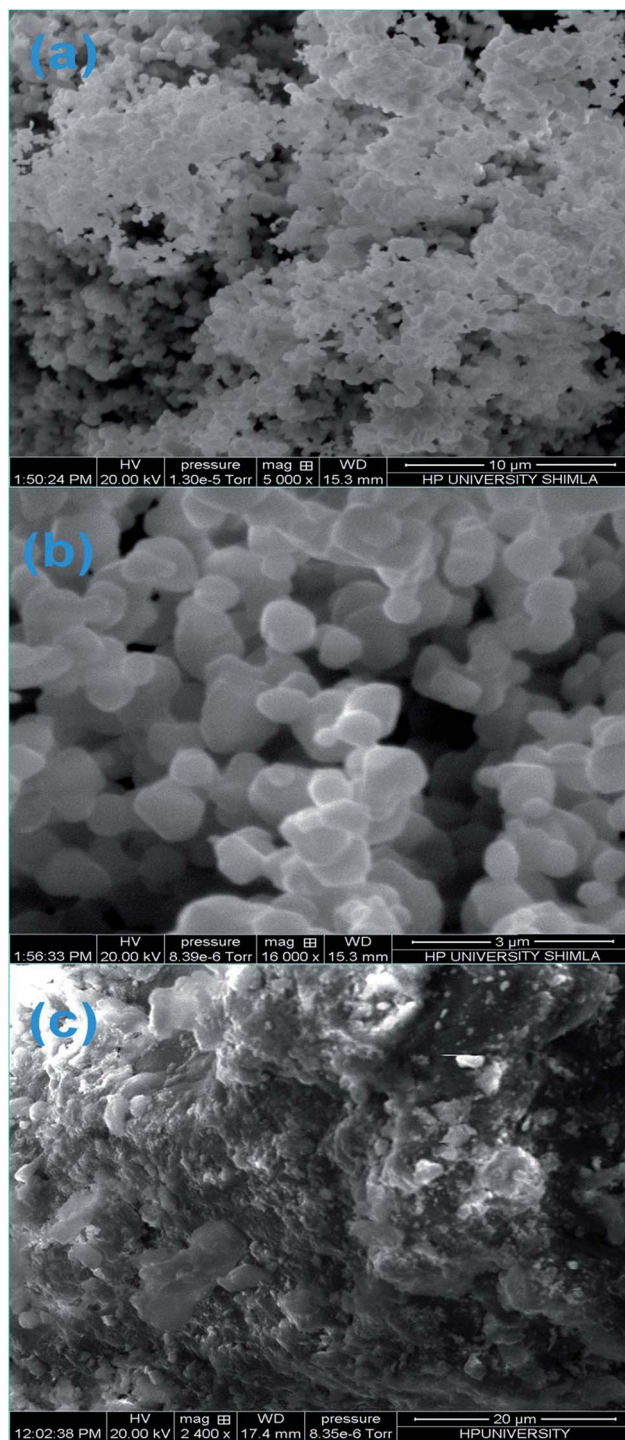

Fig. 3 (a) Low resolution SEM image of ZF, (b) high resolution image of ZF, and (c) SEM image of ZFC.

shows the clear presence of lattice fringes. The TEM images of ZrO_2/Fe_3O_4/chitosan (ZFC) are given in Fig. 6c and d. The TEM image shows that the ZF nanoparticles are uniformly distributed in the chitosan matrix. The average particle size is between 23 and 29 nm. The SAED pattern (Fig. 6b inset) of ZFC indicates that the core of the composite is nanocrystalline and all the information agrees well with the XRD results.
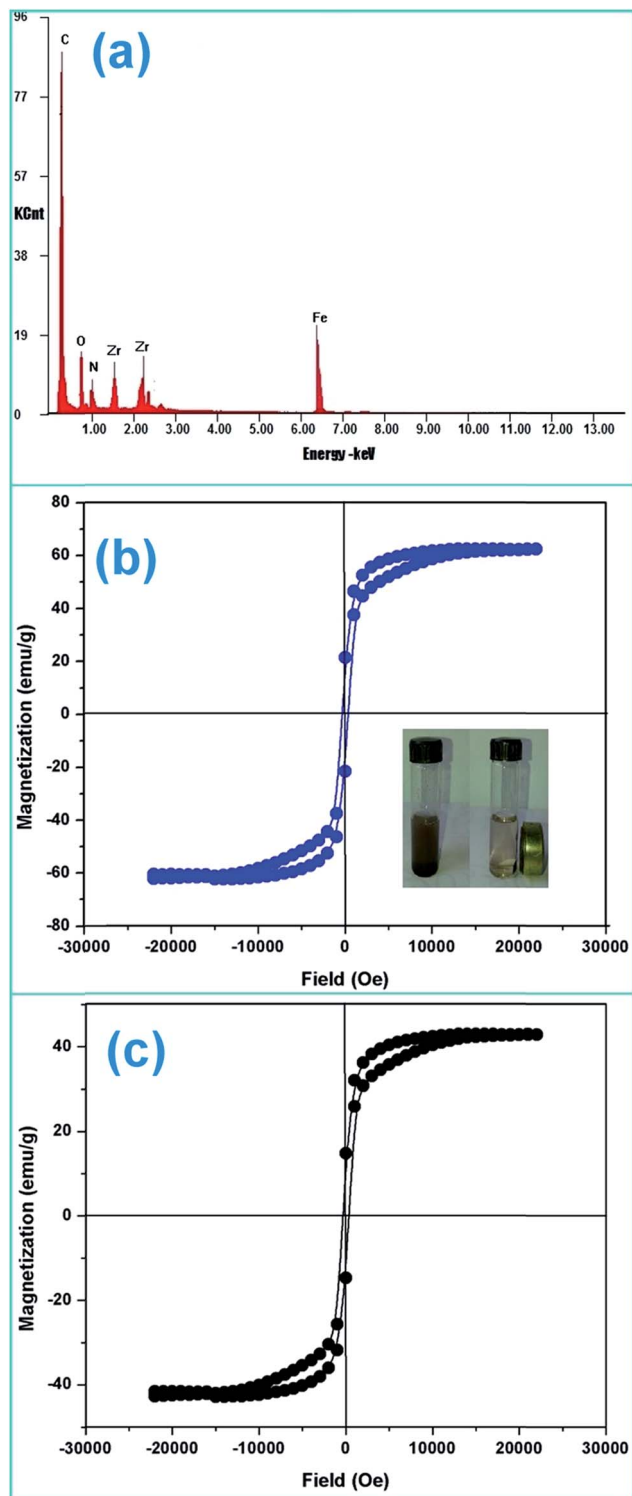
Fig. 4 (a) EDX pattern of ZFC, (b) M−H curve for ZF and (c) M−H curve of ZFC.

Fig. 5 (a) Tauc plots, (b) N_2 adsorption–desorption isotherms for ZF and (c) N_2 adsorption–desorption isotherms for ZFC.

3.2 Photoreduction of chromium (VI)

3.2.1 Photoreduction by ZF and ZFC. Fig. 7a shows the photocatalytic reduction of Cr(VI) by ZF and ZFC under visible light in aqueous solution as a function of the decrease in absorbance 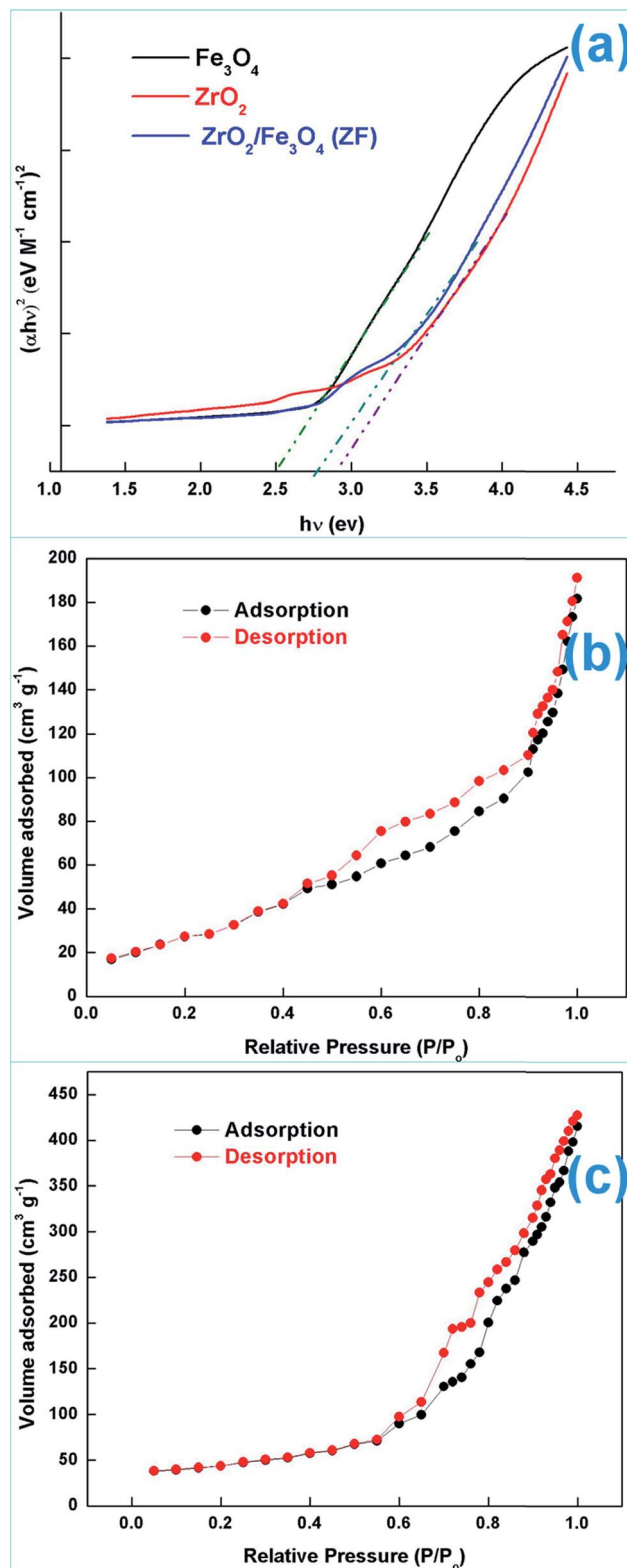of DPC-Cr(VI). A decent reduction of 71.2% was achieved in the presence of ZF. But with ZFC as the photocatalyst 84.7% of Cr(VI) was reduced under solar irradiation. In a typical mechanism due to the generation of electrons and

Table 1 Band gap parameters for ZF

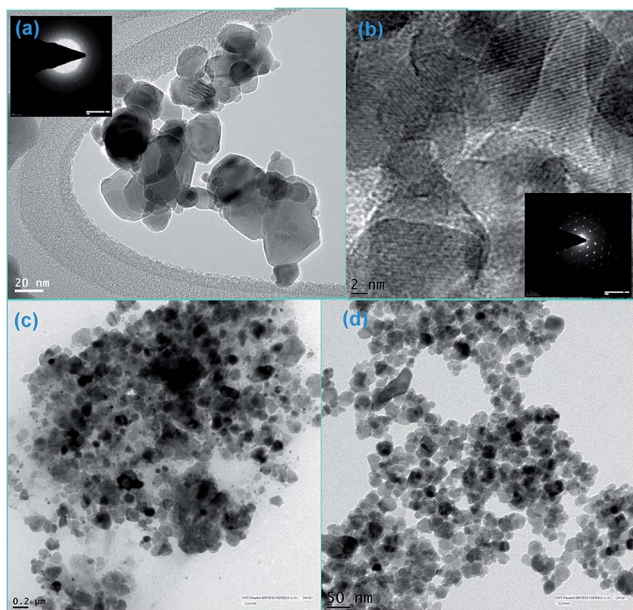| Sample	X (PAE)	E_{VB} (eV)	E_{CB} (eV)	E_g (eV)
ZrO_2	5.59	2.49	−0.30	2.82
Fe_3O_4	5.80	2.55	0.12	2.50

Fig. 6 (a) Low resolution TEM image of ZF (SAED inset), (b) HRTEM image of ZF, (c) low resolution TEM image of ZFC, and (d) HRTEM image of ZFC (SAED inset).
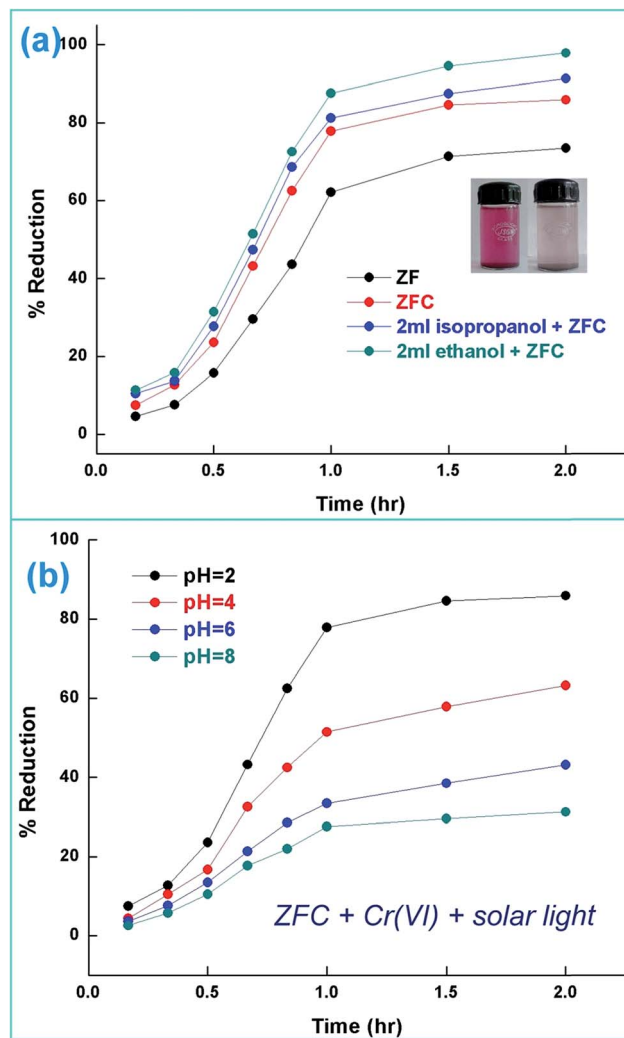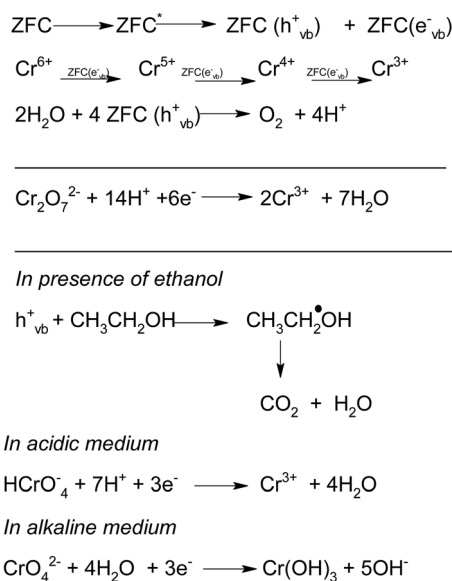

Fig. 7 (a) Photoreduction of Cr(VI) under solar light [initial pH 2], Cr(VI) = 70 mg L^{-1} [temperature = 30 ± 0.5 °C] and (b) ZFC performance as photocatalyst with pH variation under solar light.

holes on solar irradiation, the ZF heterostructure reduces the Cr(VI) into Cr(III) ions. Fig. S1(a)† shows the magnetic separation of the photocatalyst from aqueous medium and Fig. S1(b)† represents the decolorisation of DPC-Cr(VI) over time indicating the photoreduction of Cr(VI) into Cr(III). When ZrO_2/Fe_3O_4 (ZF) is irradiated by light with a photon energies $h\nu > E_g$, excitation of electrons from the valence band to the conduction bands takes place, also leading to the formation of holes. The electrons (e_{VB}) and holes (h_{CB}) lead to the reduction of dichromate ions Cr(VI) to Cr(III) and the oxidation of water to O_2.[48] A typical mechanism is represented in Scheme 1.

ZrO_2 and Fe_3O_4 exhibit slightly different band edge positions as reported by many in previous experiments. For ZrO_2/Fe_3O_4 (ZF) nano-heterojunctions the electrons in the VB can be excited to its CB with simultaneous generation of holes in its VB. The typical arrangement as obtained from band edge data shows the formation of a type-II heterojunction.[49] The CB band edge of Fe_3O_4 (0.12 eV) is positive as compared to that of ZrO_2 (−0.30 eV). There is a flow of electrons from the conduction band of ZrO_2 to the conduction band of Fe_3O_4 (the band gap of Fe_3O_4 is lower, so it shows higher absorbance and transition of electrons). On the other hand, we observe from Table 1 that as the valence band of ZrO_2 is less positive (2.49 eV) than that of Fe_3O_4 (2.55 eV), there is a movement of holes from the VB of Fe_3O_4 to the VB of ZrO_2. Thus simultaneously a charge separation is

created and facilitation of movement of charge carriers is obtained. In addition the chances of electron–hole combination are reduced. The more efficient separation of e$^-$ and h$^+$ can increase their lifetimes and enhance the efficiency of their transfer to the adsorbed substrates.[50–52] Generally, only some of the photo-excited electrons and holes migrate to the surface of the photocatalyst and react with water and O_2 to produce ˙OH groups and ˙O_2^- reactive oxygen species. On the other side other electrons and holes recombine with generation of heat. However in the case of the ZrO_2/Fe_3O_4 heterojunction there is a simultaneous charge separation and charge transfer, minimizing this combination. Due to this inter-semiconductor hole and electron transfer mechanism, the photogenerated charge carriers can be separated efficiently. So such mixed or hetero-nano-semiconductors can be employed for photodegradation of pollutants or photoreduction under solar light. As per Scheme 1, electrons reduce Cr(VI) and simultaneously holes oxidize water to oxygen. The larger movement of electrons and lower recombination thus bring out better photocatalytic

$$ZFC \longrightarrow ZFC^* \longrightarrow ZFC\,(h^+_{vb}) \;+\; ZFC(e^-_{vb})$$

$$Cr^{6+} \xrightarrow{ZFC(e^-_{vb})} Cr^{5+} \xrightarrow{ZFC(e^-_{vb})} Cr^{4+} \xrightarrow{ZFC(e^-_{vb})} Cr^{3+}$$

$$2H_2O + 4\,ZFC\,(h^+_{vb}) \longrightarrow O_2 \;+\; 4H^+$$

_____

$$Cr_2O_7^{2-} + 14H^+ + 6e^- \longrightarrow 2Cr^{3+} + 7H_2O$$

_____

In presence of ethanol

$$h^+_{vb} + CH_3CH_2OH \longrightarrow CH_3C\overset{\bullet}{H}OH$$

$$\downarrow$$

$$CO_2 \;+\; H_2O$$

In acidic medium

$$HCrO_4^- + 7H^+ + 3e^- \longrightarrow Cr^{3+} + 4H_2O$$

In alkaline medium

$$CrO_4^{2-} + 4H_2O + 3e^- \longrightarrow Cr(OH)_3 + 5OH^-$$

Scheme 1

results in the ZF heterojunction. In the case of ZFC higher reduction is observed due to the coupled case of adsorption and photocatalysis, as in general adsorption of the pollutant facilitates the degradation.[53,54] The chitosan is a good adsorbent which leads to adsorption of Cr(VI) onto its surface (at lower pH, the surface of chitosan will be less negative and thus facilitates the adsorption of $Cr_2O_7^{2-}$ on to the surface of ZFC). As soon as Cr(VI) is adsorbed on to the surface it is photoreduced by the electrons. So we achieve higher results in the case of ZFC. According to the BET studies the surface area of ZFC is higher than that of ZF. Hence there is higher adsorption and a large surface for the photocatalytic process.

The effect of the addition of isopropanol and ethanol as hole scavengers is also given in Fig. 7a. It was observed that the higher reduction of 98.5% and 92.4% was achieved in the presence of ZFC and 0.2 mL of ethanol and isopropanol respectively. As given in Scheme 1, the alcohol scavenges the holes to produce alcohol free radicals which may mineralize to CO_2 and water during the course of the reaction. CO_2 was evolved in the present study. CO_2 gas generation was observed during the degradation reaction of the BPA in the presence of the nanomaterials. CO_2 gas was identified by a saturated $BaCl_2$ solution test *via* white $BaCO_3$ precipitate formation. Because of hole depletion the recombination of electrons and holes is prevented leading to an accelerated photoreduction by electrons. Both ZF and ZFC were easily separated magnetically from aqueous solutions and reused. The generated Cr(III) may be adsorbed on to the photocatalyst and removed from the system.

3.2.2 Effect of pH on Cr(VI) photoreduction. Fig. 7b exhibits the influence of pH on the photocatalytic process. It is observed that the reduction of chromium (VI) is accelerated by lowering of the pH. A photoreduction of 84.7%, 61.2%, 40.5% and 28.7% was achieved in the presence of ZFC at pH 2, 4, 6 and 8 respectively. According to Scheme 1 it can be inferred that at extreme acidic pH, the results are better and poor reduction is

observed at basic pH. Our results are in accordance with previous findings reporting that the metal ion reduction is closely related to the pH of the solution.[55] The surface of the metal oxides as well as chitosan is positive at acidic pH and negative at higher pH. So the functional groups such as –OH and –NH_2 would be present as –OH_2^+ and –NH_3^+ on the photocatalyst surface. Therefore, the anionic species such as $Cr_2O_7^{2-}$, CrO_4^{2-}, and $HCrO_4^-$, will be deposited or adsorbed well in the acidic pH on the photocatalyst. Alternatively we can say that the lower pH would protonate the surface of the adsorbent to a higher extent. This results in stronger attraction between the negatively charged DPC-Cr(VI) with the photocatalyst. It is not only the case that the pH influences the functionality of the photocatalyst but also the chemistry of Cr(VI). In Scheme 1 it can be seen that Cr(VI) can occur in the form of $Cr_2O_7^{2-}$, $HCrO_4^-$, CrO_4^{2-}, and CrO_3 *etc*. In acidic medium $HCrO_4^-$ is predominant but in basic medium other forms become active.[56]

3.3 Photodegradation of 4-chlorophenol

3.3.1 Adsorption and catalytic degradation of 4-CP under solar light. Fig. 8a shows the photodegradation of 4-chlorophenol in the presence of ZF and ZFC under solar illumination. It was noticed that a degradation of 66% and 88.56% was achieved in the presence of ZF and ZFC respectively in a 3 h experiment. The composite shows better results. The catalyst was separated easily from the aqueous solution by the use of an external magnet. Fig. S1(a)† depicts the magnetic separation of the catalyst. The gradual disappearance of the absorption band at 280 nm with time (Fig. S2†) confirms the degradation of 4-CP in the presence of the photocatalyst.

In a typical mechanism (Scheme 2), there is generation of electron–hole pairs in the semiconductor heterostructure with solar illumination. The photogenerated holes interact with water to produce ˙OH which attack the 4-CP to remove chlorine (dechlorination) and produce 1,4-benzenediol. The reaction may further proceed to the formation of 1,2,4-benzenetriol which, *via* various further steps, leads to mineralization into simpler inorganic moieties. It is well established that many reactive oxygen species such as ˙OH, ˙O_2^-, and HO_2˙ and h^+ (shown in Scheme 2) are responsible for photocatalytic oxidation reactions, among which ˙OH is generally found to be the major reactive oxygen species. The lower band gap of 2.4 eV of the ZF heterostructure facilitates higher absorbance of visible light which forms a major part of natural sunlight.

As explained earlier there is formation of a heterojunction with the inter-semiconductor flow of charge carriers which leads to better charge separation, lower recombination and higher absorbance of visible light. The holes play an important role in the formation of hydroxyl radicals which are crucial for dechlorination. The flow of holes from the VB of Fe_3O_4 to the VB of ZrO_2 facilitates the easy availability of charge carriers and high absorbance. Thus the heterojunction of semiconductors shows higher photocatalytic activity. The results in terms of charge separation and carrier facilitation on formation of the heterostructure are pictorially represented in Fig. 9a. ZFC and ZF are completely magnetically recoverable.
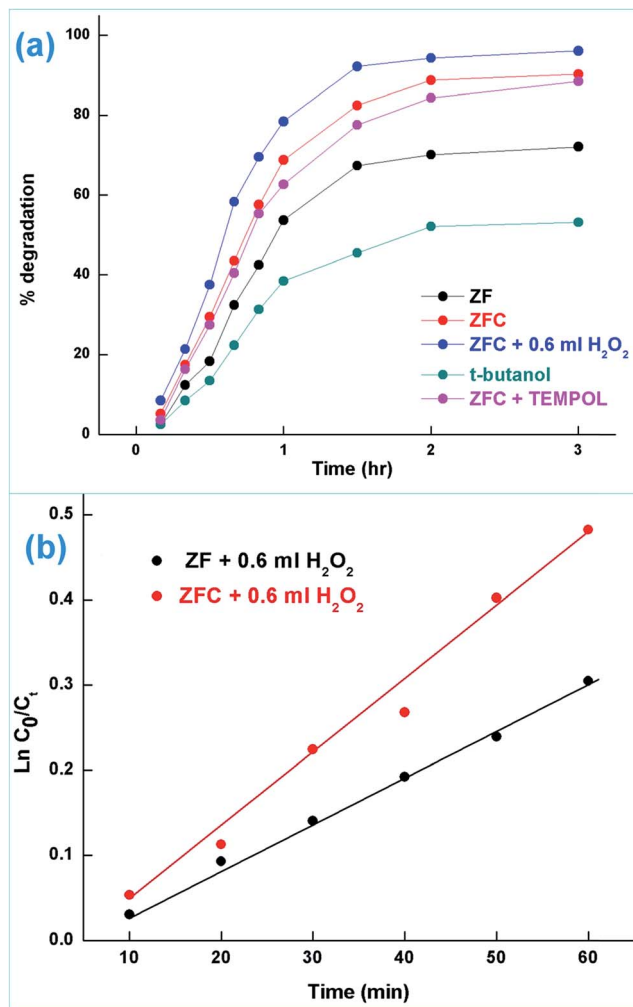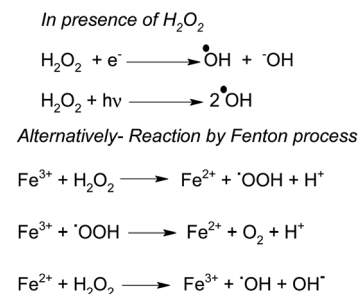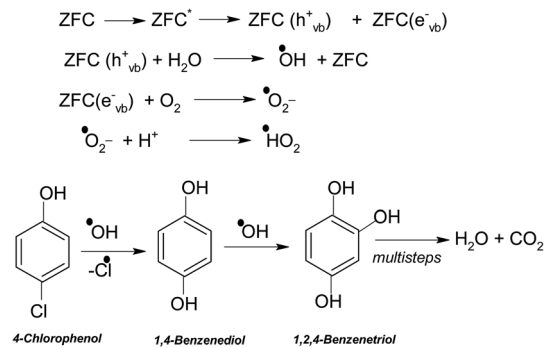
Fig. 8 (a) Degradation of 4-CP under solar light and (b) kinetics plots for 4-CP degradation by ZF and ZFC in the presence of H_2O_2 under solar light (initial pH = 5.5, initial conc. of 4-CP = 20 mg L^{-1}, and temperature = 30 ± 0.5 °C).

Scheme 2

In the case of ZFC, the chitosan plays an important role in the overall degradation process. We observe (Fig. S3†) that the ZF nanoparticles exhibit negligible adsorption of 7.3% in 1 h dark experiments, while 22% of 4-CP gets adsorbed in 1 h onto ZFC. The adsorption of CP onto the photocatalyst (ZFC) increases the rate of photodegradation. The hydroxyl groups and primary amino groups on the surface of chitosan provide a large number of adsorption sites.[57] Gel electrophoresis was used to determine the polarity of ZF and ZFC in the pH range 5–6. ZFC showed a displacement toward the positively charged electrode under the applied potential, suggesting that the surface of the nanocomposite is predominantly negatively charged.

The effect of initial pH on the photodegradation of 4-CP was also studied (Fig. S3b†) in the pH range 4–8 in the presence of ZFC. It was observed that maximum degradation is achieved at pH = 5.5. The degradation is lower at a lower and higher pH.

As per Scheme 3 the amino groups on the surface of chitosan are protonated at a lower pH of 5.5 and 4-chlorophenol exists as an anion at this pH. These positively and negatively charged species lead to a weak bond formation between the two. If we increase the pH beyond 6 the amino groups will no longer remain protonated and will decrease the adsorption. However at a lower pH phenol will be in the protonated form and would inhibit the bonding with the chitosan matrix. Similarly at a higher pH the amino groups of chitosan would either be in the neutral form or as an anion. In this case also the adsorption will not be favored. At medium pH, the superoxide radicals generated by interaction of the electrons with adsorbed oxygen react with H^+ to produce hydroxyl radicals.[58]

At highly acidic pH there is the possibility of more hydrogen ions being adsorbed onto the catalyst and thus decreasing the degradation process. Also at a sufficiently lower pH leaching of the catalyst can also be a reason for poor results.

In the case of degradation in the presence of ZFC adsorption and the photocatalytic process occur simultaneously. The adsorption process facilitates degradation of organic pollutants as the adsorbed molecule is more prone to attack by radicals. As soon as 4-CP is adsorbed onto the surface of ZFC it gets degraded. Thus ZFC shows higher degradation. The total concentration of CP at any time is:[53]

$$C = C_b + C_s \qquad (4)$$

where C_b and C_s are the amount of pollutant in the bulk and on the surface, respectively.

The amount of CP adsorbed onto the photocatalyst is given as:
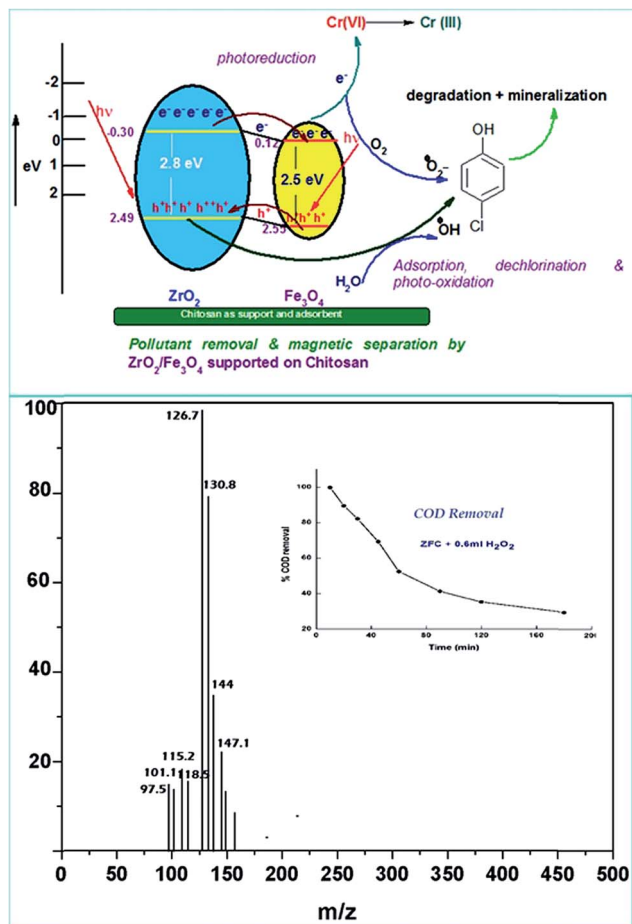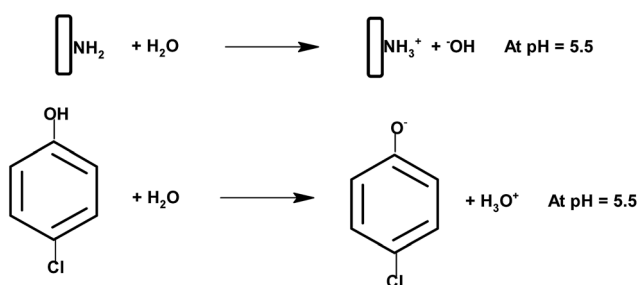
$$C_S = C_o - C_e \frac{V}{m} \qquad (5)$$

Fig. 9 (a) Band gap structure for the ZrO_2–Fe_3O_4 heterostructure and mechanism of Cr(VI) reduction and 4-CP removal and (b) mass spectrum of the solution containing 4-CP after 1 hour of degradation under solar light in the presence of ZFC (inset: COD removal in the presence of ZFC).

Scheme 3

where V is the volume of solution and m is the mass of the adsorbent.

In the presence of 0.6 mL H_2O_2 and ZFC the highest degradation of 95.4% of 4-CP was achieved in 3 h of solar illumination. Hydrogen peroxide is attacked by electrons from the valence band forming $\cdot OH$ or on absorption of light it also produces hydroxyl radicals. This will augment the degradation process. Alternatively due to the presence of Fe^{3+}, Fe^{2+} and H_2O_2

the reaction may follow the Fenton process (as per Scheme 2) and enhance the degradation or mineralization. The overall degradation process of 4-CP in the presence of ZF + H_2O_2 and ZFC + H_2O_2 follows pseudo first order kinetics (Fig. 8b). The rate constants calculated from the kinetics graphs for 4-CP degradation are 0.00432 min^{-1} ($R^2 = 0.989$) and 0.00874 min^{-1} ($R^2 = 0.996$) respectively. This shows that the degradation of 4-CP in the presence of ZFC is almost twice as fast as that with ZF.

3.3.2 Mechanistic pathway of degradation. As per Scheme 2 the main species responsible for the dechlorination and oxidation is $\cdot OH$. To confirm this the same degradation experiment was performed in the presence of 2 mL *t*-butanol and ZFC under solar light. The results are given in Fig. 8a. It was observed that the degradation was decreased to 46.5%. Tertiary butanol is a well known $\cdot OH$ radical scavenger (Scheme 4) and has been utilized in many previous experiments to confirm the role of hydroxyl radicals in photocatalytic processes.[34] The decrease in the degradation on the addition of a scavenger (*t*-butanol) is in accordance with previously reported work.

In the presence of H_2O_2 the degradation increases. However if we further increase the dosage of H_2O_2 it may behave as a $\cdot OH$ scavenging species as per Scheme 5.

We have also studied the effect of the $\cdot O_2^-$ scavenger 4-hydroxy-2,2,6,6-tetramethylpiperidinyloxy (TEMPOL) on the degradation of 4-CP in the presence of ZFC. Scheme 4 shows the reaction of scavenging of the superoxide radical anion by TEMPOL. It was observed that a very small decrease in degradation was achieved. It shows that $\cdot O_2^-$ also participates in the degradation process. But hydroxyl free radicals are the main oxidation species. Our experiment results support the fact that hydroxyl free radicals are the main species involved. However other species may also participate in the process. Hydroxyl radicals prove to be a major charge carrier and a mechanism based on that has been predicted.

In order to confirm the predicted mechanism and degradation of 4-CP, LC-MS was performed after 1 hour of solar illumination in the presence of the ZFC + H_2O_2 system. The mass spectrum is given in Fig. 9b. As per Scheme 2, the dechlorination of 4-CP leads to the formation of 1,4-benzenediol and 1,2,4-benzenetriol. The signal at $m/z = 118$ (near to 117) belongs to hydroxyl-hydroquinone (HHQ), and those at $m/z = 115$ (near to

Scheme 4

$$H_2O_2 + \cdot OH \longrightarrow \cdot HO_2 + H_2O$$

$$HO_2\cdot + \cdot OH \longrightarrow H_2O + O_2$$
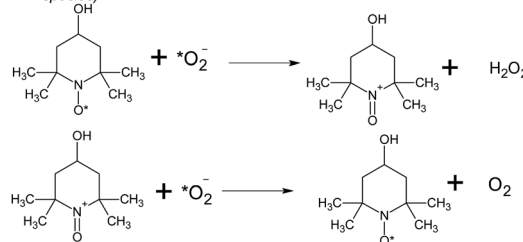
Scheme 5

110) and at $m/z = 126.7$ are for 1,2,4-benzenetriol. The degradation pathway may be the same as that reported by Li et al. in 1999.[59] The other major compounds detected are listed in Table 2. This is represented in Scheme 1.

The treatment performances for dechlorination and photodegradation of 4-CP were also evaluated using chemical oxygen demand (COD) analysis. By COD analysis it is possible to measure the total quantity of oxygen required to oxidize organic matter to simpler moieties such as water and carbon dioxide. Fig. 9b (inset) shows the reduction in COD of 4-CP at various reaction times under solar light in the presence of the ZFC + H_2O_2 system. It was observed that the COD of the solution reduced to 37% in 3 h. It proves that significant mineralization takes place which is also confirmed by the CO_2 emission

Table 2 Structures of intermediates detected in the LC–mass spectrum

S. No	m/z	Structure
1	126 (126.7)	
2	144 (144)	
3	128 (130.7)	
4	(127) 115.2	
5	90 (97)	
6	128 (118.5)	

detected by the saturated $BaCl_2$ test. The photocatalysts ZF and ZFC are magnetically separated from the aqueous medium and are reused.

4. Stability and reusability

The pollutant removal capacity and reusability of ZF and ZFC for the reduction of Cr(vi) and degradation of 4-chlorophenol was also evaluated. The photoreduction percentage of Cr(vi) for ZF (Fig. 10a) was reduced from 72.1% to 69.2% after 6 consecutive cycles. However for the composite ZFC the results were better as the reduction decreased from 87.14% to 85.1%. In each cycle the nano-photocatalyst was easily separated magnetically and reused. In a similar way the reusability study

Fig. 10 (a) Reusability of ZF and ZFC for Cr(vi) reduction and (b) reusability of ZF and ZFC for 4-CP degradation under solar light.

of ZF and ZFC was also done for the dechlorination and photodegradation of 4-chlorophenol under solar light (Fig. 10b). A degradation of 91% was achieved for the first cycle for ZFC and for the sixth cycle 87.1% was achieved. In the case of 4-CP degradation in the presence of ZF under sunlight, 71.2% degradation is achieved for the first cycle and 67.3% for the sixth cycle. The decrease in photocatalytic activity on subsequent usages may be due to accumulation of intermediates and pollutant molecules on the surface of the photocatalyst leading to a decrease in reactive oxygen species. The ZFC nanostructures are stable, reusable and magnetically recoverable.

5. Conclusions

A magnetically recoverable nano-photocatalyst ZrO_2/Fe_3O_4/chitosan was developed for multi-pollutant removal which is able to overcome the shortcomings of other current materials and pollution mitigation techniques. The semiconductor metal oxide heterojunction in low dosages is efficient in photoreduction and oxidation because of charge separation, charge transfer and lower recombination. In addition the chitosan matrix provides support, surface area and an adsorbent base for faster degradation of pollutants. The ZrO_2/Fe_3O_4/chitosan nanocomposite was able to reduce 84.7% of carcinogenic Cr(vi) in 2 h of solar illumination and the results were enhanced in the presence of ethanol. We also achieved good results for the removal of 4-chlorophenol under natural solar light as a degradation of 88.16% was obtained with a further increase by addition of hydrogen peroxide. The magnetically recoverable photocatalyst was reusable for 6 consecutive cycles with decent photo-activity. The most probable mechanisms were also predicted and supported. From this laboratory-scale experiment, a chitosan supported nano-heterojunction with promising visible light-activated photocatalytic activity for Cr(vi) and 4-chlorophenol waste water treatment with efficient utilization of solar energy was obtained.

Acknowledgements

References

1 C. Hao, J. Li, Z. Zhang, Y. Ji, H. Zhan, F. Xiao, D. Wang, B. Liu and F. Su, *Appl. Surf. Sci.*, 2015, **331**, 17–26.

2 Q. Sun, H. Li, S. Zheng and Z. Sun, *Appl. Surf. Sci.*, 2014, **311**, 369–376.

3 S. Kant, S. Kalia and A. Kumar, *J. Alloys Compd.*, 2013, **578**, 249–256.

4 L. Das and J. K. Basu, *J. Ind. Eng. Chem.*, 2015, **24**, 245–250.

5 Z. Khodami and A. Nezamzadeh-Ejhieh, *J. Mol. Catal. A*, 2015, **409**, 59–68.

6 X. F. Gao, W. T. Sun, Z. D. Hu, G. Ai, Y. L. Zhang, S. Feng, F. Li and L. M. Peng, *J. Phys. Chem. C*, 2009, **113**, 20481–20485.

7 M. Khanmohammadi, A. B. Garmarudi, H. Elmizadeh and M. B. Roochi, *J. Ind. Eng. Chem.*, 2014, **20**(4), 1841–1844.

8 L. Ge and J. Liu, *Appl. Catal., B*, 2011, **105**, 289–297.

9 J.-R. Fu, J. Zheng, W.-J. Fang, C. Chen, C. Cheng, R.-Y. Yan, S.-G. Huang and C.-C. Wang, *J. Alloys Compd.*, 2015, **650**, 463–469.

10 S. Kalia, S. Kango, A. Kumar, Y. Haldorai and R. Kumar, *Colloid Polym. Sci.*, 2014, **292**, 2025–2052.

11 C. Alanis, R. Natividad, C. Barrera-Diaz, V. Martínez-Miranda, J. Prince and J. S. Valente, *Appl. Catal., B*, 2013, **140–141**, 546–551.

12 H. T. Hsu, S. S. Chen and Y. S. Chen, *Sep. Purif. Technol.*, 2011, **80**, 663–669.

13 J. Shang, W. Hao, X. Lv, T. Wang, X. Wang, Y. Du, S. Dou, T. Xie, D. Wang and J. Wang, *ACS Catal.*, 2014, **4**(3), 954–961.

14 M. Owlad, M. K. Aroua, W. A. W. Daud and S. Baroutian, *Clean: Soil, Air, Water*, 2009, **200**, 59–77.

15 S. Huang, L. Gu, N. Zhu, K. Feng, H. Yuan, Z. Lou, Y. Li and A. Shan, *Green Chem.*, 2014, **16**, 2696–2705.

16 Y. Yang, G. Wang, Q. Deng, D. H. L. Ng and H. Zhao, *ACS Appl. Mater. Interfaces*, 2014, **6**, 3008–3015.

17 Y. Ku and I. L. Jung, *Water Res.*, 2001, **35**, 135–142.

18 H. Yu, S. Chen, X. Quan, H. M. Zhao and Y. B. Zhang, *Environ. Sci. Technol.*, 2008, **42**, 3791–3796.

19 E. D. Sherly, J. Judith Vijaya and L. John Kennedy, *Chin. J. Catal.*, 2015, **36**, 1263–1272.

20 J. Theurich, M. Lindner and D. W. Bahnemann, *Langmuir*, 1996, **12**, 6368–6376.

21 P. Rangsunvigit, R. Tharathonpisutthikul, S. Chavadej and E. Gulari, *Chem. Lett.*, 2012, **41**, 1371–1373.

22 L. J. Xu and J. L. Wang, *Appl. Catal., B*, 2013, **142–143**, 396–405.

23 V. Janda and M. Svecova, *Chem. Listy*, 2000, **94**, 905–908.

24 Y. Peng, S. He, J. Wang and W. Gong, *Radiat. Phys. Chem.*, 2012, **81**, 1629–1633.

25 M. Czaplicka, *Sci. Total Environ.*, 2004, **322**, 21–39.

26 C. Cheng, A. Amini, C. Zhu, Z. Xu, H. Song and N. Wang, *Sci. Rep.*, 2014, **4**, 4181.

27 L. Ciccotti, L. A. S. do Vale, T. L. R. Hewer and R. S. Freire, *Catal. Sci. Technol.*, 2015, **5**, 1143–1152.

28 K. K. Singh, K. K. Senapati, C. Borgohain and K. C. Sarma, *J. Environ. Sci.*, 2015, DOI: 10.1016/j.jes.2015.01.035.

29 Y. Bessekhouad, R. Brahimi, F. Hamdini and M. Trari, *J. Photochem. Photobiol., A*, 2012, **248**, 15–23.

30 Z. Wu, H. Wang, Y. Xue, B. Li and B. Geng, *J. Mater. Chem. A*, 2014, **2**, 17502–17510.

31 A. Safavi and S. Momeni, *J. Hazard. Mater.*, 2012, **201–202**, 125–131.

32 Z. Yang, X. Gong and C. Zhang, *Chem. Eng. J.*, 2010, **165**(1), 117–121.

33 A. Kumar, G. Sharma, M. Naushad and S. Thakur, *Chem. Eng. J.*, 2015, **280**, 175–187.

34 J. Si, S. B. Desu and C. Y. Tsai, *J. Mater. Res.*, 1994, **9**(7), 1721.

35 A. Caballero, J. J. Morales, A. M. Cordon, J. P. Holgado, J. P. Espinos and A. R. Gonzales-Elipe, *J. Catal.*, 2005, **235**, 295.

36 P. Egger, G. D. Soraru and S. Dire, *J. Eur. Ceram. Soc.*, 2004, **24**, 1371–1374.

37 Y. M. Li, D. H. He, Z. X. Cheng, C. L. Su, J. R. Li and Q. M. Zhu, *J. Mol. Catal. A: Chem.*, 2001, **175**, 267–275.

38 P. Berger, N. Adelman and K. Beckman, *J. Chem. Educ.*, 1999, **76**, 943–948.

39 Z. Akmar, Z. Zainoha, S. Salmijah and W. Azlina, *J. Hazard. Mater.*, 2007, **146**, 30–38.

40 APHA, *Standard Methods for the Examination of Water and Wastewater*, American Water Works Association, New York, 1989.

41 L. A. Prez-Magueda and E. Matijevic, *J. Nanopart.*, 2013, **2013**, 7.

42 G. Qui, Q. Wang, C. Wang, W. Lau and Y. Guo, *Ultrason. Sonochem.*, 2007, **14**, 55–61.

43 S. Schlabach, D. V. Szabó, D. Vollath, P. de la Presa and M. Forker, *J. Alloys Compd.*, 2007, **434–435**, 590–593.

44 M. Jason, H. J. Kim, J. Dong-Ho and Y. R. Kyong, *Carbon Letters*, 2012, **13**(2), 126–129.

45 I. Yamaguchi, K. Tokuchi, H. Fukuzaki, Y. Koyama, K. Takakuda, H. Monma and J. Tanaka, *J. Biomed. Mater. Res.*, 2001, **55**(1), 20–27.

46 S. Kant, D. Pathania, P. Singh, P. Dhiman and A. Kumar, *Appl. Catal., B*, 2014, **147**, 340–352.

47 C. Chang, L. Zhu, S. Wang, X. Chu and L. Yue, *ACS Appl. Mater. Interfaces*, 2014, **6**, 5083–5093.

48 Y. C. Zhang, J. Li and H. Y. Xu, *Appl. Catal., B*, 2012, **123–124**, 18–26.

49 R. Marschall, *Top. Curr. Chem.*, 2015, 1–30.

50 J. Su, L. Guo, N. Bao and C. A. Grimes, *Nano Lett.*, 2011, **11**, 1928–1933.

51 D. Sarkar, C. K. Ghosh, S. Mukherjee and K. K. Chattopadhyay, *ACS Appl. Mater. Interfaces*, 2013, **5**, 331–337.

52 Y. P. Yuan, S. W. Cao, Y. S. Liao, L. S. Yin and C. Xue, *Appl. Catal., B*, 2013, **140–141**, 164–168.

53 A. Kumar, G. Sharma, M. Naushad, S. Kalia and P. Singh, *ACS Ind. Eng. Chem. Res.*, 2014, **53**, 15549–15560.

54 D. Pathania, G. Sharma, A. Kumar, M. Naushad, S. Kalia, A. Sharma and Z. A. Alothman, *Toxicol. Environ. Chem.*, 2015, **5**, 526–537.

55 T. Iwata, M. Ishikawa, R. Ichino and M. Okido, *Surf. Coat. Technol.*, 2003, **169–170**, 703–706.

56 N. Tewari, P. Vasudevan and B. K. Guhas, *Biochem. Eng. J.*, 2005, **23**(2), 185–192.

57 K. Inoue, K. Yoshizuka and K. Ohto, *Anal. Chim. Acta*, 1999, **388**, 209–218.

58 N. Venkatachalam, M. Palanichamy, B. Arabindoo and V. Murugesan, *J. Mol. Catal. A*, 2007, **266**, 158.

59 X. Li, J. W. Cubbage, T. A. Tetzlaff and W. S. Jenks, *J. Org. Chem.*, 1999, **64**(23), 8509–8524.